

Radiation and Scattering of EM Waves in Large Plasmas Around Objects in Hypersonic Flight

Original

Radiation and Scattering of EM Waves in Large Plasmas Around Objects in Hypersonic Flight / Scarabosio, A.; Araque Quijano, J. L.; Tobon, J.; Righero, M.; Giordanengo, G.; D'Ambrosio, D.; Walpot, L.; Vecchi, G.. - In: IEEE TRANSACTIONS ON ANTENNAS AND PROPAGATION. - ISSN 0018-926X. - STAMPA. - 70:6(2022), pp. 4738-4751. [10.1109/TAP.2022.3142310]

Availability:

This version is available at: 11583/2963011 since: 2022-05-09T15:06:17Z

Publisher:

Institute of Electrical and Electronics Engineers Inc.

Published

DOI:10.1109/TAP.2022.3142310

Terms of use:

This article is made available under terms and conditions as specified in the corresponding bibliographic description in the repository

Publisher copyright

IEEE postprint/Author's Accepted Manuscript

©2022 IEEE. Personal use of this material is permitted. Permission from IEEE must be obtained for all other uses, in any current or future media, including reprinting/republishing this material for advertising or promotional purposes, creating new collecting works, for resale or lists, or reuse of any copyrighted component of this work in other works.

(Article begins on next page)

Radiation and Scattering of EM Waves in Large Plasmas Around Objects in Hypersonic Flight

A. Scarabosio, J. L. Araque Quijano, J. Tobon *Member, IEEE*, M. Righero, G. Giordanengo, D. D'Ambrosio, L. Walpot and G. Vecchi *Fellow, IEEE*

Abstract—Hypersonic flight regime is conventionally defined for $\text{Mach} > 5$; in these conditions, the flying object becomes enveloped in a plasma. This plasma is densest in thin surface layers, but in typical situations of interest it impacts electromagnetic wave propagation in an electrically large volume. We address this problem with a hybrid approach. We employ Equivalence Theorem to separate the inhomogeneous plasma region from the surrounding free space via an equivalent (Huygens) surface, and the Eikonal approximation to Maxwell equations in the large inhomogeneous region for obtaining equivalent currents on the separating surface. Then, we obtain the scattered field via (exact) free space radiation of these surface equivalent currents. The method is extensively tested against reference results and then applied to a real-life re-entry vehicle with full 3D plasma computed via Computational Fluid Dynamic (CFD) simulations. We address both scattering (RCS) from the entire vehicle and radiation from the on-board antennas. From our results, significant radio link path losses can be associated with plasma spatial variations (gradients) and collisional losses, to an extent that matches well the usually perceived blackout in crossing layers in cutoff. Furthermore, we find good agreement with existing literature concerning significant alterations of the radar response (RCS) due to the plasma envelope.

Index Terms—Hypersonic plasma, antennas in plasmas, plasma scattering, re-entry vehicles

I. INTRODUCTION AND MOTIVATION

Hypersonic flight regime is conventionally defined for $\text{Mach} > 5$, also called hypervelocity regime; it is the standard condition of vehicles re-entering Earth atmosphere from various orbits, or entering extra-terrestrial atmospheres (e.g. Martian). It is also the physical condition of (proposed) future transport [1], [2], of meteors (asteroids entering Earth atmosphere) [3], [4] and de-orbiting space debris (that must be monitored for safety). A very recent addition is the proposal, and in some case fielding, of hypersonic weapon systems [5].

In these physical conditions, the extreme shock wave due to hypervelocity generates intense heat and ionization of atmospheric gases. When this happens, the flying object is enveloped in the resulting plasma, often with a significant trailing wake.

This plasma may generate significant effects on the radio communication between the vehicle and ground or satellite

relay links, as well as on access to Global Navigation Satellite Systems (GNSS). As well known, when the link direction crosses plasma layers with plasma frequency near or above the link frequency, a significant path loss emerges, usually called “blackout”; lower levels of attenuation are often called “brownout”. Likewise, the plasma may significantly impact the radar return, in the first place its Radar Cross Section (RCS). For meteor-type objects, the plasma also constitutes the ionized trailing tail, that allows its radar observation [4].

In typical conditions where the plasma has significant effects on radiation and scattering of EM waves, most flying objects and the plasma cloud around it (including the wake) are electrically large, and the plasma is inhomogeneous throughout.

Full-wave methods have been reported for this problem. Volume integral equations (VIE) are a natural choice for these inhomogeneous dielectrics surrounding mostly impenetrable airframes, also because they can be accelerated, and reported in several works [6]–[12]. However, plain application of VIE for these plasmas pose significant issues of stability, addressed in [6]–[8]. A discontinuous Galerkin method has been proposed in [11], [12]; the numerical examples in these relevant works have (correctly) focused on situations that were mostly critical for the respective methods; as a result, simple and relatively thin plasma layers have been considered there. Finite Difference Time Domain (FDTD) can also be employed, with time convolution because of the associated dispersion; examples are in [13], [14], and application to realistic re-entry cases is reported in [15], requiring supercomputing facilities (45M unknowns).

In order to emulate situations happening in reality, the plasma distribution must come from computational fluid dynamic (CFD) simulations; these take as input the flying object shape and materials, the local atmosphere, and the flight trajectory; most relevant are the velocity and angle of attack. The trajectory may be known with accuracy for re-entering space vehicles, estimated for meteor-like objects, or largely unpredictable (which is conspicuously the case for hypersonic weapons [5]). Similar considerations can be made for the shape and materials of the hypersonic objects, with the additional observation that CFD boundary conditions depend on coating materials (e.g. ablative or non ablative thermal shields).

Even when the trajectory is known with accuracy, and so are the geometry and materials of the object, uncertainties remain in the CFD predictions, as CFD boundary conditions are known from experimental datasets, and subject to Ansatz and assumptions. Finally, the possible onset of turbulence

A. Scarabosio, M. Righero and G. Giordanengo are with the LINKS Foundation, Via P. C. Boggio, 61 - Turin, Italy, (email: andrea.scarabosio@linksfoundation.com).

J. Tobon, D. D'Ambrosio and G. Vecchi are with the Politecnico di Torino, Corso Duca degli Abruzzi, 24 - Turin, Italy.

J. L. Araque Quijano is with the Universidad Nacional de Colombia, Bogota, Colombia.

L. Walpot is with European Space Agency - ESA, Paris, France.

and its characteristic lengths may generate fluctuations in the electron densities with impact on the EM response.

Overall, the plasma and hence its EM effect have to be considered to some degree stochastic [16], [17]. On the most-deterministic end, one would like to consider error bars in the results, via a sensitivity analysis. In the most uncertain case, the results ideally should come from a Monte Carlo process.

As a result, the case emerges for approximate and numerically nimble simulation approaches; they can - inter alia - allow for parametric studies, ideally up to Monte Carlo characterization of the EM quantities of interest in the prediction endeavour.

In this scenario, numerical methods based on asymptotic approximation of plasma propagation are good candidates to compromise between accuracy and computational load, as will be discussed in this work.

In this sense, our approach is inspired by the foundational work in [18], [19]. Those ideas, with some modifications and additions, are applied in this work to full 3D plasmas arising from CFD simulation of real flying objects; an extensive validation is performed prior to addressing EM characterization of a real-life atmospheric re-entry vehicle in hypersonic flight regime. This real-life study case is the European Space Agency (ESA) IXV re-entry vehicle (shown in Fig. 1); more information about the IXV vehicle and the related ESA mission can be found in [20], [21] and references therein.

Different approaches based on high-frequency approximations have also been reported in recent works for plasmas [22], [23], and for other dielectric media with conductive insertions [24].

The paper is organized as follows. In Sec. II we describe the physical and numerical model; Sec. III describes the validation of the method, and finally an application to an actual re-entry vehicle is reported in Sec. IV.

Preliminary accounts of the present work were presented in conference publications [25]–[27].

II. PHYSICAL AND NUMERICAL MODEL

A. Plasma model: CFD model

The hypersonic flow about a re-entry vehicle is computed by solving the full Navier-Stokes equations for multi-component gas mixtures. The physical model includes species mass balance equations, and vibrational energy balance equations to account for high-temperature effects. The gas mixture is assumed to be composed of 11 species, namely O_2 , N_2 , O , N , NO , O_2^+ , N_2^+ , O^+ , N^+ , NO^+ and e^- . Chemical reaction rates are taken from [28], [29], and the transport model is based on the Chapman-Enskog method and it adopts the collisional integrals suggested in [30], [31], [31]–[33]. The governing equations are discretised according to a finite volumes method. Convective fluxes are evaluated using standard upwind flux-difference splitting techniques, and diffusive fluxes through a centered scheme. Second order accuracy in space and in time is achieved using an Essentially Non-Oscillatory scheme. Chemical source terms are treated implicitly to avoid instabilities due to fast chemical reactions.

In the following, the plasma and gas thermodynamic quantities are calculated according to the model in [34], [35]. The

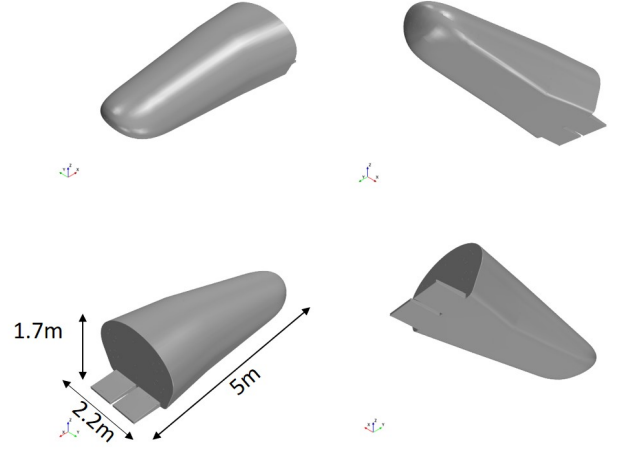


Fig. 1. CAD rendering of the ESA IXV re-entry vehicle.

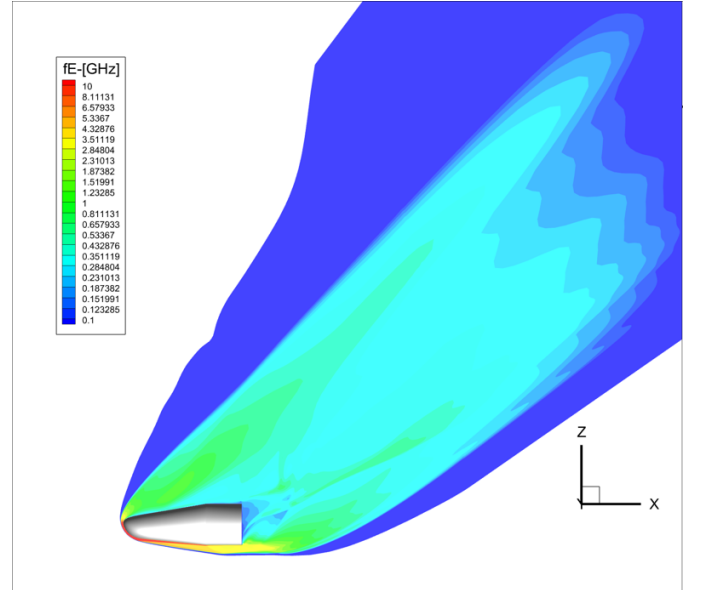


Fig. 2. Plasma around the IXV vehicle during re-entry flight at Mach number 15, the figure depicts density as plasma frequency.

model accounts for gas ionisation by shock waves due to the hypersonic flow. We stress the fact that these first principle calculations are already quite realistic and constitute the state-of-the-art for shock waves generated plasmas simulations.

A typical result, for an actual re-entry vehicle is shown in figure 2.

B. Plasma model: EM model

Throughout this work the medium is supposed to be stationary; a time-dependence $\exp(-i\omega t)$ in the EM fields is assumed and suppressed, with $\omega = 2\pi f$ being the angular frequency at frequency f .

We are interested in the frequency range where the plasma response is dominated by the electron motion; we do consider collisional effects in the plasma and neutral particles, but as the wave phase velocity is much greater than plasma thermal velocity, temperature and higher order collective kinetic effects

can be left out. This is the so-called collisional unmagnetised “cold plasma” approximation in standard literature. In this regime the dielectric tensor is diagonal and the proper plasma constitutive relation is [36]:

$$\epsilon_r(\mathbf{r}) = 1 - \frac{\omega_{pe}^2(\mathbf{r})}{\omega(\omega - i\nu_c(\mathbf{r}))} \quad (1)$$

where $\omega_{pe}^2 = n_e e^2 / (\epsilon_0 m_e)$ is the electron plasma frequency (squared), n_e the electron density, m_e the electron mass, ϵ_0 the vacuum permittivity and ν_c is the neutral-plasma collision frequency. Equation (1) is also equivalent to well-known Appleton-Hartree equation (in the special case of no magnetic field), which has been extensively applied to ionospheric propagation [37]. For multi species partially ionised plasmas the collision frequency is related to temperature via [38]:

$$\nu_c(\mathbf{r}) = \sum_{\alpha} n_{\alpha,0}(\mathbf{r}) \sigma_{\alpha,c}(T_e(\mathbf{r})) \sqrt{\frac{8k_B T_e(\mathbf{r})}{\pi m_e}} \quad (2)$$

with T_e being the electron temperature, n_0 the neutral density, k_B the Boltzmann constant and $\sigma_{\alpha,c}$ is the neutral-electron scattering cross section for the neutral specie α . The collisional frequency is a function of T_e through both the electron mean velocity and the scattering cross section. Accurate fits of cross sections data, relevant for a hot air plasma, can be found in [33] and are used here for the calculation of ν_c . In a single ideal gas approximation a representative value of σ_c for hot air is $1 \cdot 10^{-19} \text{ m}^2$ [33], [39].

In our model, the spatial distribution of the hypersonic flow and of the related plasma parameters are known in numerical form from CFD simulations. Hence, data representation must be made consistent with the EM model. As detailed in Sec. II-D, we need to compute both the relative electric permittivity and its gradient for a very high number of spatial locations; due to data origin, the gradient has to be computed numerically. If not done with care, this step may lead to inaccurate EM field calculation and/or very high computational cost. Moreover, the plasma profiles are typically computed in CFD simulation on an unstructured spatial grid. Most of the accurate and fast multivariate interpolation methods are available for regular gridded data set only, which makes the gradient calculation a critical data processing. We choose to process the CFD 3D plasma profiles in two steps. First, we interpolate $\epsilon_r(\mathbf{r})$ on a regular rectangular grid with typical resolution of $\approx \lambda/5$. Second, we fit the regular grid using a global cubic spline, that allows a rapid and smooth evaluation of the gradient, which is continuous by construction. This process is performed only once and the spine fitting is used to compute the r.h.s. of eq. 5 during trajectory integration (see section II-D).

C. Modelling Strategy

The overall physical model of the scattering problem is shown in Fig. 3. We have one or more impenetrable objects (in black) immersed into an inhomogeneous medium (coloured map) defined by the dielectric function $\epsilon(\mathbf{r})$ (possibly complex).

The source can be internal to the inhomogeneous dielectric, as is the case for an antenna on a vehicle, or external, such as an incident plane wave, as it is the case for RCS computations.

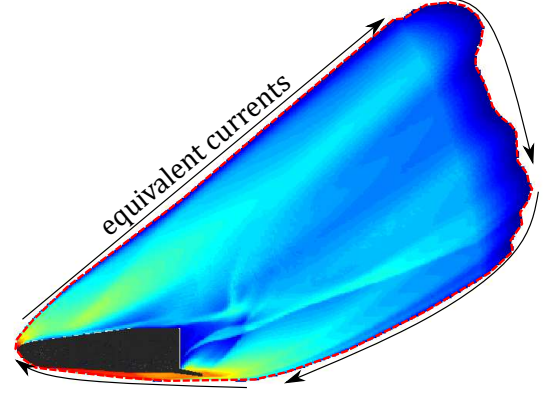


Fig. 3. Schematic of the physical model. Inhomogeneous media (here plasma surrounding a vessel) are enclosed by an equivalent surface (dashed red line) on which equivalent currents radiate to the outside. Note the large extension of the plasma volume.

We employ Equivalence Theorem to separate the inhomogeneous region from the surrounding free space via an equivalent (Huygens) surface. The scattered field is obtained via free space radiation of the magnetic and electric surface equivalent currents $\mathbf{M}_s = -\mathbf{n} \times \mathbf{E}$ and $\mathbf{J}_s = \mathbf{n} \times \mathbf{H}$, where the \mathbf{E} and \mathbf{H} are the electric and magnetic fields on the equivalence surface, and \mathbf{n} is the surface normal unit vector.

We are especially concerned with situations where the plasma volume is electrically large, as is typical in most cases of interest, and its density varies slowly compared to the operational wavelength λ ; hence, we employ the Eikonal approximation [40]–[42] to Maxwell equations in the inhomogeneous region; note that the mentioned use of the Equivalence Theorem does not involve any approximation for radiation outside the inhomogeneous region.

Rays originate either from the antenna location (radio link case) or from outside the plasma region (RCS case). There is no physical discontinuity between plasma and free space, avoiding the need to generate both reflected and refracted rays at interfaces. Regardless of their origin point, rays are followed until they intersect the equivalent surface, where their contribution to the (equivalent) field is calculated. For the case of incident wave source, where rays start outside the equivalent surface, both entrance and exit intersections are considered. Once the fields at the equivalent surface are calculated by ray-tracing, they are converted to surface current via the Equivalence Theorem and made radiate in free space generating the far total (radio link case) or scattered (RCS case) field.

It is now appropriate to briefly discuss the choice of the equivalence surface. The Eikonal solution is an approximate one, and thus it is convenient to limit its region of application as much as possible; hence, the equivalence surface is chosen to enclose only points where plasma effects are not negligible (from that point outwards, radiation is exact). This can be implemented in the ray propagation scheme described below in

Sec. II-D by stopping the rays where such a condition happens. However, there are situations where rays encounter caustics, and on such surfaces the field approximation is inaccurate; when this happens close to the equivalence surface (see e.g. the discussion in Sec. III-A2), it is then necessary to move such a surface outwards.

Finally we observe that in case material discontinuities with penetrable materials need to be modeled, they can be taken into account by using the Fresnel transmission and reflection coefficients, and following both the reflected and refracted rays [19].

D. Propagation within the vehicle-plasma region

To compute the EM wave propagation into inhomogeneous media we use the classical Eikonal theory [41]. The Eikonal field approximation can be expressed as follows:

$$\mathbf{E}(\mathbf{r}) = \mathbf{e}(\mathbf{r})E(\mathbf{r})e^{ik_0S(\mathbf{r})} \quad (3)$$

where $E(\mathbf{r})$ is a slowly varying field, \mathbf{e} is the unit polarisation vector, and $S(\mathbf{r})$ is the normalised Eikonal phase function (defining the wave-front surface). This Ansatz is inserted into Maxwell equations, with the assumption that the medium properties are weakly dependent on the spatial coordinate (see below for discussion of validity), which yields the hierarchy of equations for the Eikonal function, energy (power density) and the polarization [40], [41]. As this is well-known, we will only list our specific choices for the numerical implementation of this set of equations. We express the ray trajectory equation as system of first order Ordinary Differential Equations (ODEs) using the normalised wave-vector $\boldsymbol{\xi} = \nabla S$ as dynamic variable and the electrical path length differential $d\sigma = \text{Re}(\sqrt{\epsilon_r}) ds$, where s is the arc-length along the trajectory; this results in:

$$\frac{d\mathbf{r}}{d\sigma} = \frac{\boldsymbol{\xi}}{\text{Re}(\epsilon_r)} \quad (4)$$

$$\frac{d\boldsymbol{\xi}}{d\sigma} = \frac{1}{2\text{Re}(\epsilon_r)} \nabla \text{Re}(\epsilon_r) \quad (5)$$

To the next order of the hierarchy, one has the power density and polarization transport, that assume the solution of the trajectory equations. The complex polarisation unit vector $\hat{\mathbf{e}}$ obeys the following equation along the ray trajectory [40]:

$$\frac{d\hat{\mathbf{e}}}{d\sigma} = - \left(\hat{\mathbf{e}} \cdot \frac{d\boldsymbol{\xi}}{d\sigma} \right) \frac{\boldsymbol{\xi}}{|\boldsymbol{\xi}|^2} \quad (6)$$

As the trajectory equations (4), this equation is integrated with standard ordinary differential equations (ODE) techniques. At a difference with previous literature [18], [19], we have chosen to use (4) and (6) because they have shown to be more stable in complex geometries as those present in actual re-entry situations, as in Sec. IV; this results from the absence of high order curve differentials that would need to be computing *after* ray tracing. Furthermore, these formulas are easily integrated into ODE solution involved in ray tracing, which enables more efficient and accurate computations.

Energy transport requires considering that the plasma is possibly lossy due to collisions; we assume weak to moderate dissipation and follow here the general procedure for

anisotropic plasma transport [43], for the special case of an isotropic plasma. The transport equation for the field energy can be cast into the form of a divergence equation [40] with a linear dissipation term coming from the anti-hermitian part of the dielectric tensor (simply $\text{Im}(\epsilon_r)$ in the isotropic case) as:

$$\nabla \cdot (v\hat{\mathbf{t}}U) = ck_0 \frac{\text{Im}(\epsilon_r)}{\text{Re}(\epsilon_r)} U \quad (7)$$

where c is the vacuum speed of light, $\hat{\mathbf{t}}$ is the unit vector along the trajectory, k_0 is the free-space wave number and $U = \text{Re}(\epsilon_r)|E|^2$ is the EM energy density in Eikonal approximation. Equation (7) shows the interplay between: 1) the divergence of rays due to the local variations of the local index 2) the energy absorption by the lossy medium, embedded in the imaginary part of ϵ_r , and 3) the wave amplitude $|E|$.

Phase and amplitude transport in our case result in the following relationship between (complex) amplitudes at two points P_1 and P_2 along a ray path:

$$E(P_2) = E(P_1) \sqrt{\frac{\text{Re}(n_2)}{\text{Re}(n_1)}} DF \exp(i\Phi - \alpha), \quad (8)$$

where $n_\ell = \sqrt{\epsilon_r(P_\ell)}$ is the complex refractive index evaluated at P_ℓ , with $\ell = \{1, 2\}$, and

$$\alpha = k_0/2 \int_\gamma \frac{\text{Im}(\epsilon_r(\mathbf{r}))}{\text{Re}(\epsilon_r(\mathbf{r}))} d\sigma, \quad \Phi = k_0 \int_\gamma d\sigma, \quad (9)$$

where γ is a parametrization of the ray trajectory between points P_1 , and P_2 , namely $\gamma : [\sigma_1, \sigma_2] \rightarrow \mathbb{R}^3$ with $\gamma(\sigma_1) = P_1$ and $\gamma(\sigma_2) = P_2$ and γ obeys to (4) and (5). In (8) DF indicates the divergence factor that accounts for divergence of the infinitesimal ray tube (i.e. along an individual ray) in a lossless medium; it represents the shrinking or expansion of the wave front surface along its propagation, and will be addressed next in Sec.II-E. The medium properties needed for evaluating the ray path and equations (8,9) are either computed from analytical models or via numerical interpolation of gridded data as explained in Sec. II-B.

1) *Discussion on Eikonal validity for hypersonic plasmas:* Following well established literature [40], [41], [43] the necessary condition for the applicability of the ray theory can be cast into the following relations:

$$\delta \equiv \frac{|\nabla \log(|\epsilon_r|)|}{k_0} \ll 1 \quad (10)$$

$$\frac{|\nabla \log(|\mathbf{E}|)|}{k_0} \ll 1 \quad (11)$$

$$\frac{\text{Im}(\epsilon_r)}{\text{Re}(\epsilon_r)} \sim \delta \quad (12)$$

The first two demand the properties of the medium and the wave amplitude to vary slowly over the distance of a wavelength (i.e. weakly dependent on the spatial coordinate \mathbf{r}). The last equation requires a weak energy exchange between the media and the EM wave and partly overlaps with eq. 11. As well known, these conditions are typically violated near caustics (even in free-space), cut-off and resonance regions. This issue are addressed in Sec.II-E2 and below. The reader

interested ray theory for more general lossy media violating eq. 12 may for instance refer to [44], [45].

In a hypersonic plasma, a high density, high gradient region may be generated near the hypersonic vessel and depending on the flight conditions (i.e. Mach number) cut-off layers appear. The ray is expected to suffer reflection at cut-off, since the wave is evanescent on the other side. Actually, reflection must occur before the cut-off is reached [46]. Indeed, for oblique propagation, only the component of \mathbf{k} parallel to the density gradient goes to zero, whereas the group velocity is still well defined. This kind of reflection does not lead to a global breakdown of the Eikonal approximation, but is associated with the formation of a caustic or of a focal point, so that some care has to be taken in the determination of the phase along the ray (see section II-E2). Thus, even in this extreme case, a good approximation is expected away from the cut-off layer (i.e. at the equivalent surface). In section IV we discuss the validity of the ray approach for each considered plasma case.

Finally, we address the issue of antenna-in-plasma modeling with the proposed method. The present interest focus is on TTC or Navigation type antennas, which are the typical application. For these relatively simple antennas a single-point source is typically enough along with its radiation pattern. Electrically larger antennas (reflectors or arrays) could be addressed with multiple source points, each with its own ray tracing. Significant near-field interaction with the plasma may lead to relevant impact on antenna input impedance, which is not considered in this work.

E. Ray-Tube approach

Because of the expected complexity of the ray set as a whole, we shift from a ray-based approach, as common in the related literature, to a ray-tube based description of the relevant field quantities. This allows to include collective effects such as ray folds (e.g. caustics) that are not directly present in the individual ray descriptors, and to express amplitude and radiation in a more effective manner. To do this, we group rays in bundles of three (see figures 4 and 6), on the basis of geometrical contiguity at launch; this only entails proper book-keeping of trajectories. Each three-ray bundle is a ray-tube in our scheme.

We begin by briefly describing the ray initialisation scheme. As a first step, the equivalence surface (ES) is converted into a triangular tessellation using standard algorithms; the triangular cells have a typical side length varying in the range from $\lambda/10$ to $\lambda/3$. As said earlier on, the equivalence surface is arbitrary and may coincide with the boundary of the scattering media. Alternatively, a canonical shape such as a sphere (see fig. 6 and 7) can be chosen to encapsulate the media volume. The nodes (vertices) of the mesh determine ray launch directions. **We note that the ES's size has a direct impact on the computational time. In fact, a larger surface leads to a) longer ray trajectories and b) larger number of launched rays (i.e. when keeping fixed the size of the patch cell relative to λ).**

For sources in the plasma region (e.g. antennas mounted on a vehicle) ray starting directions are obtained by the directions of the vertices of the equivalent surface mesh as seen from

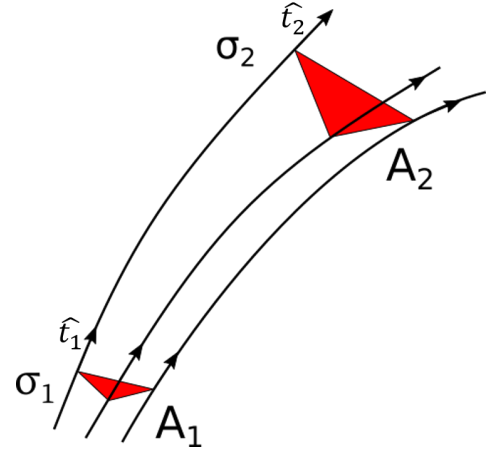


Fig. 4. Sketch of the adopted ray tube propagation scheme.

the source location. For a plane wave source, rays start all parallel from a plane just outside the equivalence surface, with initial direction normal to the starting plane; their location (and density) is determined by back-projecting the mesh nodes along the wave direction onto the starting plane.

The initial associated field intensity and polarisation may be sampled from input antenna data or may be provided in analytical form. In figure 6 we show a set of rays (red lines) launched from a point just above a simple vessel (black), in free space. The rays point toward the spherical equivalence surface nodes and they are stopped at the intersection.

Rays that encounter the impenetrable vessel (or any other such body) are reflected, i.e. they are stopped and re-launched with new initial conditions according to the usual specular reflection laws and the appropriate Fresnel reflection coefficients. Figure 7 shows an example of the electric field on the equivalence surface.

1) Amplitude and Radiation: Convenience of the ray-tube description is immediately evident for the amplitude calculation, and the ensuing radiation. The divergence factor (DF) appearing in amplitude propagation (8) can in principle be expressed in terms of the local surface principal radii (see for example [42]). Although mathematically exact, this formulation contains higher order derivatives of the Eikonal function which may be subject to large error when the medium properties are not known analytically but resulting from other numerical calculations or measurements, as in our CFD-originating plasmas. We prefer instead to estimate DF directly from the wave front evolution of the three-ray tubes introduced above (see figures 4 and 6). With reference to the notation of Fig. 4, we have that the divergence factor can be related to the changes in the front surface area simply with the relation $DF = \sqrt{A_1/A_2}$.

At a difference with other approaches [18], [19], the radiated field is obtained consistently with the ray-tube based approach described above. That means that the (far) radiated field is expressed as the sum of the radiation from the patches ΔT_i defined by the intersection of the ray tubes with the chosen

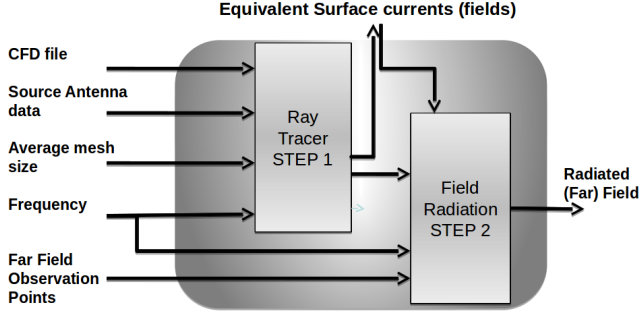


Fig. 5. Algorithm overview with input and output data.

equivalence surface,

$$\mathbf{E}_s(r, \theta, \phi) = \sum_i \mathbf{E}_{s,i}(r, \theta, \phi) \quad (13)$$

an example of these patches is shown in the simple case of Fig. 7.

The field on each triangular patch is approximated with constant magnitude and linear phase variation. The electric field vector \mathbf{E}_i is obtained as the average of the three values pertinent to the three rays of any tube, as per (8), (6) (note that the divergence factor is intrinsically a tube property, while phase, attenuation and polarization are properties of individual rays). The magnetic field \mathbf{H}_i is likewise obtained from the three values at the rays, in turn related to the electric field there by the local ray impedance relationship, and the wavefront normal $\hat{\mathbf{t}}_i$ is likewise the average of the three ray wave front normals.

With these assumptions, the patch radiated fields can be expressed as:

$$\mathbf{E}_{si}(r, \theta, \phi) = \frac{-ik_0}{4\pi} \frac{e^{ik_0 r}}{r} e^{-ik_0 \hat{\mathbf{r}} \cdot \mathbf{r}_i} S_i(\theta, \phi) \mathbf{a}_i \quad (14)$$

with

$$\begin{aligned} \mathbf{a}_i &= \hat{\theta}(-\hat{\phi} \cdot \mathbf{M}_i + \hat{\theta} \cdot Z_0 \mathbf{J}_i) + \hat{\phi}(\hat{\theta} \cdot \mathbf{M}_i + \hat{\phi} \cdot Z_0 \mathbf{J}_i) \\ S_i(\theta, \phi) &= \frac{1}{\Delta T_i} \int_{\Delta T_i} e^{ik_0(\hat{\mathbf{r}} - \hat{\mathbf{t}}) \cdot (\mathbf{r}' - \mathbf{r}_i)} d\Sigma' \\ \mathbf{M}_i &= -\hat{\mathbf{n}}_i \times \mathbf{E}_i, \quad \mathbf{J}_i = \hat{\mathbf{n}}_i \times \mathbf{H}_i \end{aligned} \quad (15)$$

where \mathbf{r}_i , $\hat{\mathbf{n}}_i$ and ΔT_i are the patch centroid, normal unit vector and the surface area respectively, $\hat{\theta}$, $\hat{\phi}$ are the unit vectors in the directions θ , ϕ and $\hat{\mathbf{r}}(\theta, \phi)$ the unit vector which points from the origin to the observation point, and Z_0 is the free space impedance. It turns out that the radiation shape factor S_i can be conveniently written in closed form [47] for quick and efficient radiation calculation.

We observe that this ray-tube based approach to radiation does not require to assign a surface area to individual rays on the equivalent surface. Also, in presence of complex inhomogeneity, tubes with rays diverging far apart are expected to have lower accuracy; as they result in larger areas, their contribution to radiated field is weaker: this results in an intrinsic robustness.

Equation (15) provides the numerical model for the radiated field, and together with the ray-tracing model in section II-D,

constitute the main components of the method proposed. In figure 5 we present a schematic overview of the implemented algorithm, consisting in two main modules: the ray-tracer module and the radiation model together with the inputs and outputs.

2) *Folds*: It is well known that the Eikonal approximation breaks down near caustics where the field becomes singular. We are, in general, not interested in the field nearby the caustics; thus, we will place the equivalent surface sufficiently far from them (although one must often compromise with other numerical constraints, see section III-A). Nevertheless, caution must be taken when a ray tube passes throughout one these singular regions. Caustics arise when the ray field folds. The wave front folding affects the phase of the field carried by the wave with a phase shift of $\pi/2$ radians. These events must be accounted for, so that the proper phase shifts can be applied to the ray tube field. Caustics may be, in principle, detected by calculating the principal radii of the wave front [19], [42], but again high order numerical derivatives can make this a very difficult task. We detect instead the crossing of rays forming the ray tube which occurs when passing through the caustic point and apply phase shift correction.

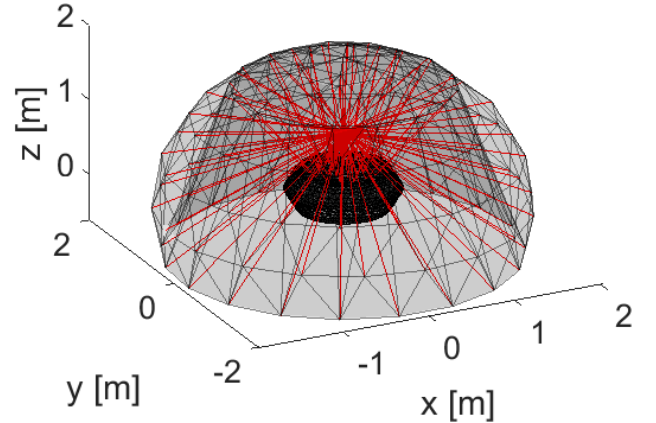


Fig. 6. Ray trajectories (red lines) from a dipole source above a small simplified vessel, in free space. The spherical equivalence surface is also depicted (coloured).

III. BENCHMARK OF NUMERICAL MODEL

Validation of the code is divided into two parts: a) against an inhomogeneous dielectric with impenetrable core with spherical symmetry; b) for complex cores in free space. Study case a) mimics the configurations of interest, a flying object enveloped in a non-homogeneous plasma, but in a geometry that affords exact results for reference. Because of availability of reference results, the spherical validation a) will be done with plane wave excitation. Conversely, free space validation b) can be done against reference Method of Moments (MoM) simulations for both simple and real-life vehicle shapes; the latter will be done especially for testing on-vessel near sources: We employ [48] to generate the MoM reference.

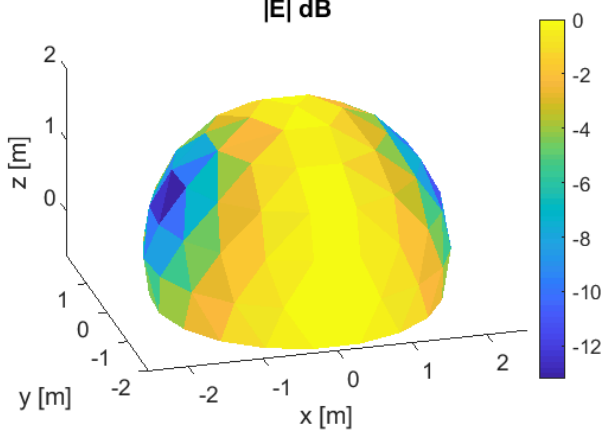


Fig. 7. Electric field on a spherical equivalent surface for the configuration in Fig. 6.

In the following, the present hybrid method will be often labelled "RT" (after Ray Tracing) for the sake of brevity.

A. Validation against spherical symmetry references

Thanks to the existence of accurate analytic solutions using the Mie series [49]–[51] for spheres we can compare our results with highly accurate references.

The electrical sizes considered in the following are on the same order of magnitude of those involved in the real-life application case in Sec. IV; as seen in Fig. 1, the IXV vehicle is enclosed in a box of size $L_1 \times L_2 \times L_3$, $L_1 = 5\text{m}$, $L_2 = 2.2\text{m}$, $L_3 = 1.7\text{m}$; at the S-band telemetry and command link frequency of 2.6GHz the electrical size of the box is $kL_1 \approx 300$, $kL_2 \approx 120$, $kL_3 \approx 90$, where $k = 2\pi/\lambda$ is the wave number.

1) *PEC sphere in vacuum*: The only physical parameter which varies in the case of a PEC sphere in free space [50], [52] is the product ka , where a is the sphere radius. As for all asymptotic methods, good results are expected for large ka . Forward and back scattering values computed with the present method are found to agree within 10% of the Mie series values when $ka > 10$ (back scattering shown in Fig. 10). Figure 8 shows the bistatic RCS the vertical or θ -polarization with $ka = 31.4$ calculated with the Mie series and the present method. The horizontal polarisation is omitted for clarity and presents similar features. Here the convention is that the plane wave (PW) propagates along $-z$, thus we have back-scattering for $\theta=0^\circ$ and forward-scattering for $\theta=180^\circ$. The diffractive interference pattern in the angular region of forward scattering (large angles) is qualitatively reproduced with decreasing accuracy toward smaller angles where oscillations between Mie and our solutions become out of phase. We notice that the results of the present method are very similar to those of Physical Optics (PO) (Fig. 9 and 10): we now explain this result. As said earlier, the location of the equivalent surface is arbitrary but best results for this case are obtained by placing the surface as close as possible to the

PEC. Under these conditions, the resulting equivalent currents are very close to the PO currents $\mathbf{J} = 2\mathbf{H}_{inc} \times \mathbf{n}$ and $\mathbf{M} = 0$ where \mathbf{H}_{inc} is the incident magnetic field and \mathbf{n} is the normal to the PEC surface. For ray fields, the total field is the sum of the incident term plus the specular reflected field. When the equivalent surface approaches PEC surface the tangent electric field $(\mathbf{E}_{inc} + \mathbf{E}_{ref}) \times \mathbf{n}$ cancels out, and the magnetic field doubles; this fact has been verified numerically using equivalent surfaces at distance $\leq 0.01\lambda$ from the PEC. Hence, the results of the proposed hybrid method are consistent with the result of PO, as this latter is actually the limit for this hybrid method in these configurations.

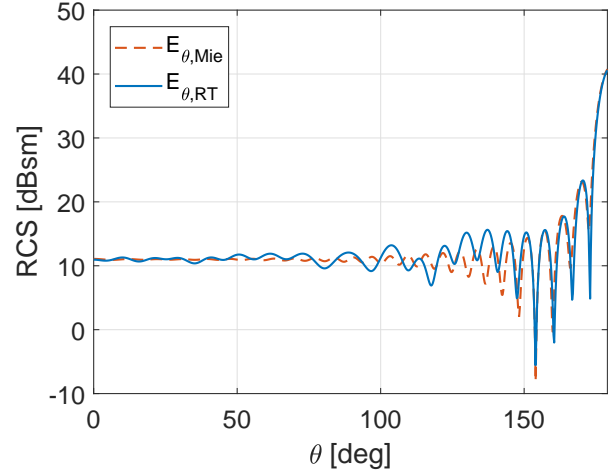


Fig. 8. Bistatic RCS of a PEC sphere for $ka = 31.44$. Comparison of present method (labelled RT) and Mie solutions.

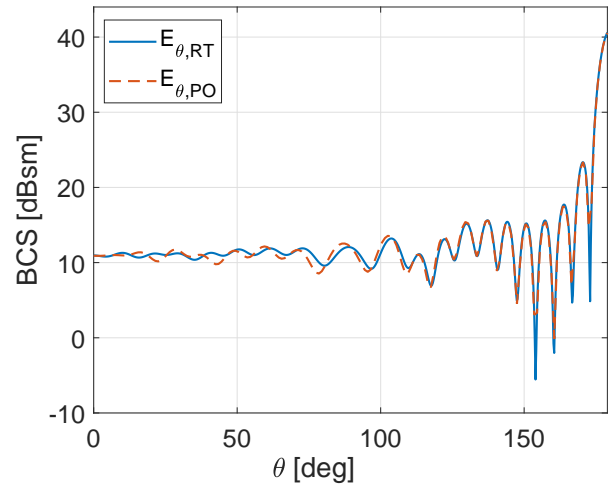


Fig. 9. Bistatic RCS of a PEC sphere for $ka=31.44$. Comparison of present method (labelled RT) and PO solutions

2) *Inhomogeneous sphere with PEC core*: We now consider an inhomogeneous dielectric surrounding a PEC core, both with spherical symmetry. Despite the simplicity of the spherical geometry, this example includes all the complex physical phenomena and conditions of a real-life case such as ray bending (due to continuous refraction), reflection and

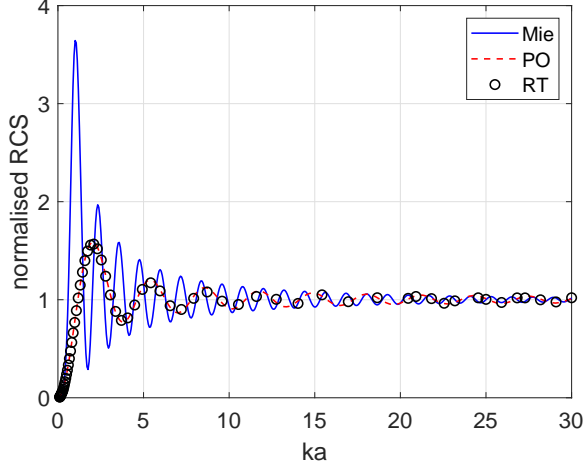


Fig. 10. RCS of a PEC sphere as function of ka . Comparison of present method (labelled RT), PO, and Mie solutions.

diffraction. Indeed, as will be seen, this is a conservative test, as the (extreme) symmetry entails special critical cases that are unlikely in more complex geometries. The dielectric has a permittivity profile given by:

$$\epsilon_r(r) = \frac{1 + \epsilon_c}{2} \left(1 - \frac{1 - \epsilon_c}{1 + \epsilon_c} \cos \left(\pi \frac{r - R_{in}}{R_{out} - R_{in}} \right) \right) \quad (16)$$

with $R_{in} = a$, $R_{out} = 3R_{in}$; we will examine scattering as a function of the relative permittivity at the core, ϵ_c . As before, we focus on electrically large objects and consider a PEC sphere with radius $ka=62$ (e.g. $a=1\text{m}$ at a frequency of $f=3\text{GHz}$). The scattering geometry and selected ray trajectories are shown in figure 11.

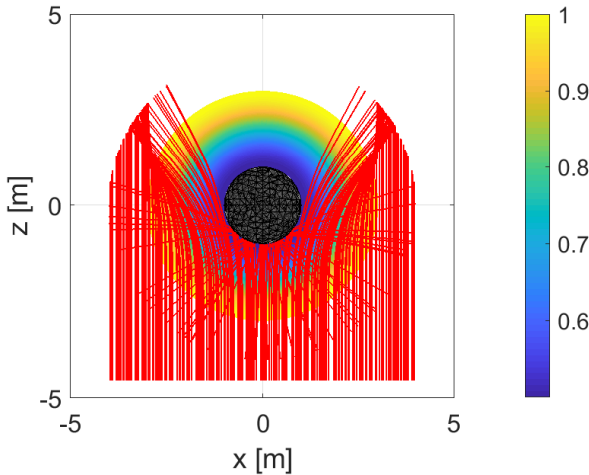


Fig. 11. Spherically inhomogeneous dielectric with PEC core, $\epsilon_r(r) < 1$: selected ray trajectories (line source). PEC sphere is in black, the colormap represents $\epsilon_r(r)$ with the profile in eq. (16) and parameters $\epsilon_c = 0.5$, $R_{out}/R_{in} = 3$, and $kR_{in} = 62$.

This dielectric profile has the effect of bending the rays away from the sphere, producing field scattering and a peaked bistatic RCS around $\theta = 0^\circ$.

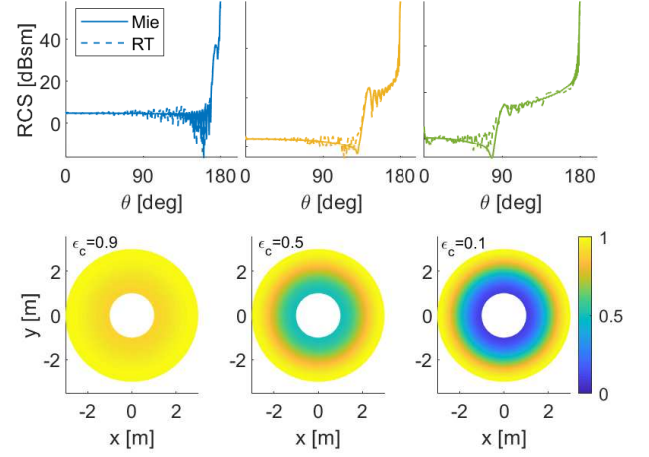


Fig. 12. Spherically inhomogeneous dielectric with PEC core, $\epsilon_r(r) < 1$: bistatic RCS for various values of minimum permittivity (ϵ_c). The colormap represents $\epsilon_r(r)$ with the profile in eq. (16) with $R_{out}/R_{in} = 3$, $kR_{in} = 62$, and for various listed ϵ_c . Upper row: RT Vs. Mie results for $\epsilon_c = 0.9-0.1$. Lower row: color map of the relative permittivity profiles.

Figure 12 displays the bistatic RCS profiles for ϵ_c in the range 0.1 – 0.9 for both the RT and Mie solution. Even at the lowest permittivity $\epsilon_c \leq 0.1$ the small parameters δ (see eq. 10) is mostly below 0.01 and never exceeds 0.05 for all traced rays, ensuring the validity of the ray tracing method. Here the convention is that the PW propagates along $-z$, thus having back-scattering for $\theta = 0^\circ$ and forward-scattering for $\theta = 180^\circ$.

There are three major qualitative changes when varying ϵ_c : 1) the back-scattering decreases for lower ϵ_c ; 2) the peak forward scattering ($\theta = 180^\circ$) increases with scattering volume but does not depend on ϵ_c (note that the PEC sphere in vacuum has $\text{RCS}_{vac}=47\text{ dBsm}$ whilst with dielectric $\text{RCS}_{die}=58\text{ dBsm}$); 3) the forward scattering profile broadens with lower ϵ_c . The same trends are also clearly visible in the RT simulations (dashed lines) and they find an easy interpretation in terms of rays. At lower ϵ_r in fact, the rays are more and more refracted away and some “miss” the PEC object (see Fig. 11) reducing back-scattering and broadening the forward scattering profile. The same mechanism is also at the basis of the plasma stealth effect for not absorbing plasmas (refraction only). Special attention and consideration is needed for solutions with lower ϵ_c . Although qualitatively satisfactory, the profiles with $\epsilon_c < 0.5$ suffer from noise and in general lower accuracy so that for those profiles in Fig. 12 we have applied some smoothing to reduce small scale spatial features (with dimension smaller than λ) in order to increase clarity. We have investigated the origin of this inaccuracy. The different ray tube contributions can be divided into: a) tubes entering into the equivalence surface, b) bent and eventually reflected exiting tubes. The analysis of these classes shows that the spurious oscillations can be attributed to the bending rays and ultimately to numerical error in the trajectories, and to the appearance of caustics. Caustics surfaces form near and within the dielectric boundary when ϵ_c falls sufficiently low.

In Fig. 11 the formation of a caustic surface can be observed just outside the outer boundary of the dielectric for $\epsilon_c = 0.5$. For an equivalent surface nearby caustics ray field amplitude is small and its evaluation inaccurate; one has then to move this surface away from the object, to have higher field accuracy. This is however sub-optimal, as the best results of the hybrid RT-surface-radiation approach are obtained by placing the equivalent surface as close as possible to the scatterer, reducing the volume where the ray approximation is applied, as discussed earlier on. For this geometry and permittivity distribution, we find a good compromise by positioning of the equivalence surface between 5λ and 10λ away from the dielectric boundary. This ‘optimal’ or trade-off surface position changes obviously with the caustics location and ultimately with permittivity. This effect is displayed in Fig. 13 where we compare the monostatic RCS from Mie series and RT. It is seen that, for $\epsilon_c \leq 0.5$, standard Huygens surface at the dielectric boundary leads to large uncertainty in the RCS value. **The error is reduced by moving the Huygens surface to the trade-off surface.** Residual error remains for the lowest ϵ_c . At a first glance one may conclude that extraction of back scattering signals is very inaccurate under these conditions. However, the solution is within the framework of the ray approximation itself by isolating the reflected-only ray tubes and their contributions to the back-scattering (see red-dotted line in Fig. 13). We conclude by stressing that the caustics issue discussed in this example is very extreme and due to the idealised spherical geometry. In real life situations ray trajectories are more chaotic, caustics are not structured, and much less of a problem.

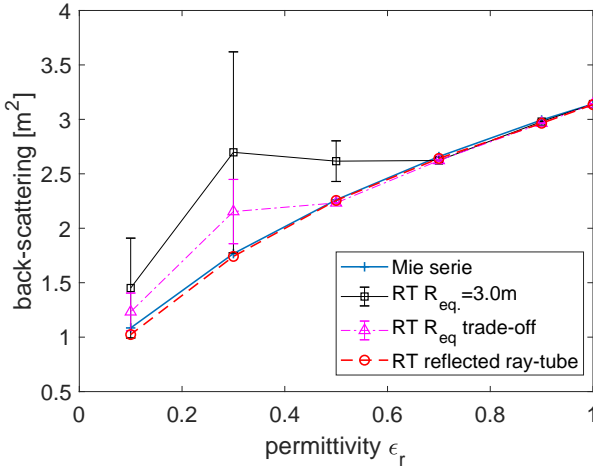


Fig. 13. Spherically inhomogeneous dielectric with PEC core, $\epsilon_r(r) < 1$: Comparison of the monostatic RCS for ϵ_c ranging from 1 to 0.1. Effect of choice of Huygens surface and ray-tube selection. Default Huygens at dielectric boundary with $R_{Huygens} = 3.0m$ in black, trade-off $R_{Huygens}$ in magenta and extraction of reflected ray-tube only in red. **Error bars represent the statistical error in the extraction of the back-scattering cross-section from θ -profile (fitting).**

B. Complex cores in vacuum: comparison with MoM

1) *Radiation from on-vehicle antennas:* In this section we benchmark the RT code with simple antennas, although

the code can take any antenna pattern as input for the ray initialisation.

Curved reflecting surfaces demand for sufficiently accurate meshing; hence, before addressing a real-life geometry, we consider a simplified vessel with surfaces both flat and with single curvature. The object is shown in the lower right of Fig. 14; it is composed of two truncated cones joined together. The top and bottom flat disks are 10λ of diameter, and the antenna is located at about 0.25λ below the bottom side. Here the antenna is constituted by 2 crossed dipoles fed to provide circular polarization.

The benchmark of the field pattern is presented in figure 14. Both polar and co-polar polarization are well calculated with the shadow region ($\theta \approx 0^\circ$) being less accurate but less important in magnitude as expected. Quantitative agreement within few percent are reached for fields 30dB down from peak value.

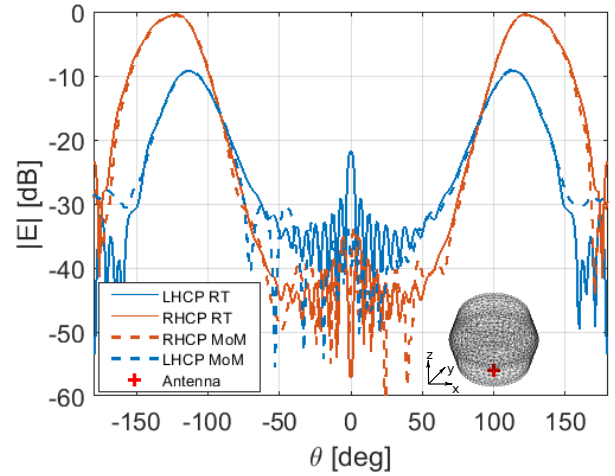


Fig. 14. Radiation of a circularly polarized source on PEC simplified core. The antenna is a pair of crossed dipoles (along x and y), with RHCP. Cut at $\phi = 0$.

Next, we consider the IXV vessel case study. The working frequency is 2.26 GHz, corresponding to the standard S-band telemetry (TM) link.

We consider here an x -oriented dipole located at top rear of the vessel (see Fig. 15) at 1.77λ distance from the surface; while not a typical antenna, it is considered to check the interference pattern from the interaction of the primary and reflected fields.

The cut at $\phi = 0^\circ$ is plotted in Fig. 15. The interference pattern in both the E_θ and E_ϕ components are fairly well reproduced. Discrepancies are visible at large angles where fields are already more than 25dB smaller than the largest value. Note that, compared to reflection on a flat surface, the peaks are shifted laterally toward larger angles and this effect is properly captured by the simulations. Not surprisingly, it is found that a proper tessellation is crucial for a correct reflection and interference simulation for curved surfaces. The typical patch size, at least in the region nearby the source should not exceed $\lambda/5$, as also typically used in MoM simulation.

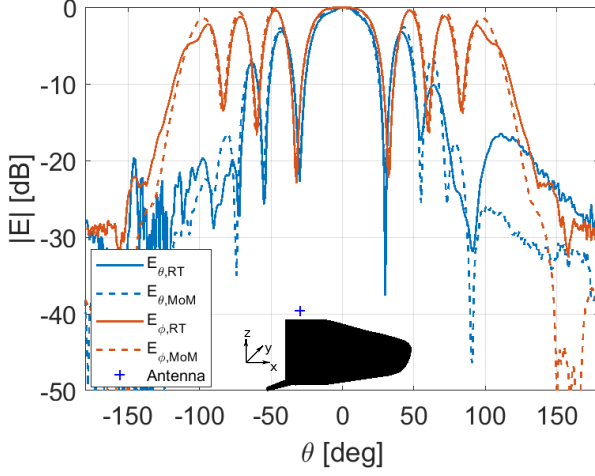


Fig. 15. Radiation of a linearly polarized source on IXV vessel; the antenna is an x-oriented dipole at 1.77λ distance from the surface. Cut at $\phi = 0$.

2) *Scattering (RCS)*: Finally we compute the differential cross-section of the ESA IXV re-entry vehicle mentioned in the Introduction; the frequency is again 2.26 GHz.

We compare the Ray-tracing simulation with both MoM and PO free space calculations. Incidence is in the plane of symmetry of the vehicle (mid-plane), from $\theta = 45^\circ$ below the vehicle axis (see Fig. 16); the z -axis is in the vertical direction (upward), with the x -axis pointing out of the drawing plane.

In Fig. 16 we compare the MoM, the RT and the PO normalised scattering cross section for $\phi = 0^\circ$. Three main peaks exist in the bistatic RCS profile, similar to what happens for a finite cylinder at oblique incidence (not shown for brevity). The peak at $\theta = 45^\circ$ is the forward scattering; that at $\theta = -45^\circ$ is the back scattering from (vertical) flat vehicle aft, as for the cap (disk) of a cylinder; that at $\theta = 135^\circ$ is the back scattering from main body, especially the bottom of the vehicle. Similar results are observed for various angles of incidence of the PW, not reported for the sake of conciseness.

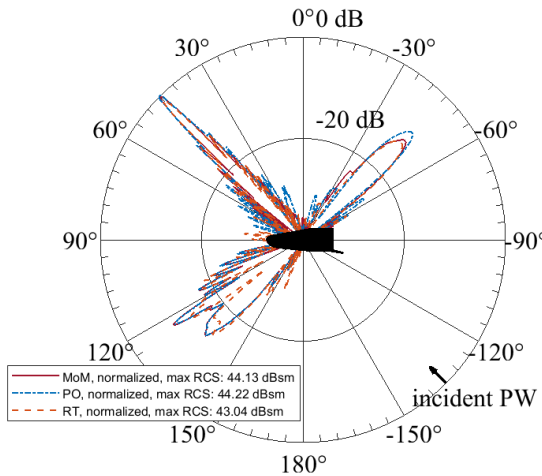


Fig. 16. IXV vessel in vacuum: bistatic RCS with incidence from $\theta = -135^\circ$. Comparison of MoM (full line), PO (dot-dashed line) and RT (dashed line) solutions.

IV. EFFECT OF PLASMA ON RCS AND ANTENNA PATTERN: THE IXV CASE

In this section we study the effect of plasma on both the scattering cross section and on the radio link for on-board antennas; we consider the plasma both including and neglecting collisional effects. We consider effects on the radio links both at the S-band telemetry and control (TM, 2.26 GHz) and L-band navigation (GPS) frequencies; we study bistatic RCS at the TM frequency, as representative of the 3-5 GHz radar band.

A. Plane wave incidence

We begin with plane-wave incidence, as it affords a simpler view of plasma-related effects.

In the first place, we consider the effects of high-density layers associated with cutoff, i.e. for which the operation frequency is near or below the local plasma frequency ω_{pe} (see (1)).

In typical re-entries, the densest plasmas are associated to thin boundary layers underneath the vehicle, and in front of the nose (as in Figs. 2 and 3). Fig. 17 depicts a small number of relevant rays (to avoid cluttering), in a flight condition where these denser layers are in cutoff at the considered frequency (TM, here). One clearly sees “reflection-type” effects (depicted in dashed blue and red colors for clarity), where dense layers appear to act on rays as a reflecting (e.g. PEC) boundary. A closer analysis shows that rays turn around before reaching the cutoff surface, and the “reflection” is actually a sharp bend (see also discussion in section II-D1). In a short section of the ray path ($< \lambda$) around reflection, both density gradient and adsorption exceed the strict validity conditions and a local Eikonal solution would result in inaccurate representation of the \mathbf{E} field. We however, seek for a solution at the equivalent surface, several meters away from cut-off where a good approximation is to be expected provided we correct for the phase shift. This explains why we did not explicitly consider such a reflection condition (which is possible, though) into the code. On the other hand, it is noted that denser layers prevent EM waves to interact with the vehicle body, and the RCS will be determined by the plasma distribution rather than the vehicle geometry.

Rays encountering lower plasma densities are also bent away from the vessel and will contribute to the scattered field in related directions.

The effect of the above wave phenomena on scattered field is seen in Fig. 18; the figure compares the bistatic RCS for the vehicle alone (i.e. in vacuum) and with the plasma envelope; It also highlights the effect of plasma collisions leading to power absorption and reduction in the scattered fields, as can be expected; it is to be observed that in the reported realistic conditions absorption effects are significant in RCS return

In a collisionless plasma (purple dashed line) the back-scattering (peak at $\theta = 135^\circ$) is shifted toward higher angles and overall reduced; this is due to the “geometric” effect of plasma, and the peak reduction is attributable to loss of coherence. The PEC reflection is replaced by reflection-like effect from plasma around cutoff, and again the beam is

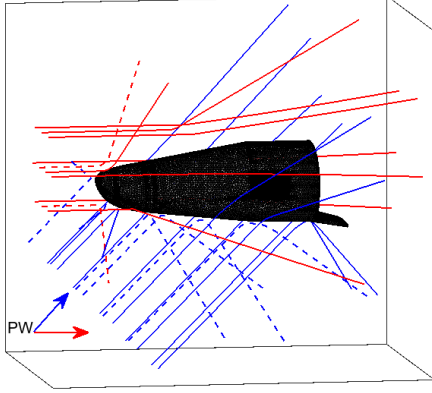


Fig. 17. IXV vehicle at Mach 12: selected ray trajectories for plane-wave illumination. The figure shows two directions of incidence. Rays in dashed lines exhibit sharp reflection-like patterns related to cut-off plasma layers underneath the vessel and in front of the nose.

more scattered than for specular coherent reflection because of inhomogeneity in the plasma volume. The other reflection peak at $\theta = -45^\circ$ is mostly unchanged in this case; this peak is due to reflection from the aft portion of the vehicle, and in this case the involved rays do not encounter a high density plasma. For higher Mach numbers, however, a high density wake plasma is formed behind the IXV vessel which impede the rays from reaching the aft flat part; in these cases (not shown) the back-scattering peak disappears. **The “geometric” effect of bending or reflecting rays is apparent by comparison to the vacuum RCS: it is well-known that the forward scattering cross section (peak at $\theta = +45^\circ$) arises from the masking/blockage size of the target. Since the plasma increases the apparent size of the target, this larger apparent size leads to a larger forward cross section.**

Collisional plasma absorption can be particularly effective under these conditions of both high plasma and neutral density. The bistatic RCS for a Mach 12 collisional plasma (blue dash-dotted line) shows a strongly reduced back scattering. The back-scattering RCS aft-related peak is reduced by several dBs but still clearly visible. For higher Mach numbers (not shown), only forward radiation survives.

B. Radio links

We now move to consider radiation from antennas mounted on the vehicle.

Fig. 19 shows the relevant ray phenomena for an antenna mounted on board under the Mach 15 condition at the telemetry channel frequency (2.26 GHz). Rays depart from the location of TM antenna, on the side of the vehicle. The figure also includes some slices that illustrate the plasma’s relative permittivity. Rays do not encounter the cut-off layer but are seen to bend toward the nearby upper region with lower plasma density (higher dielectric constant), as can be seen from the density maps. The high density and gradients are localised in a narrow region near the antenna and vessel surface. Even there,

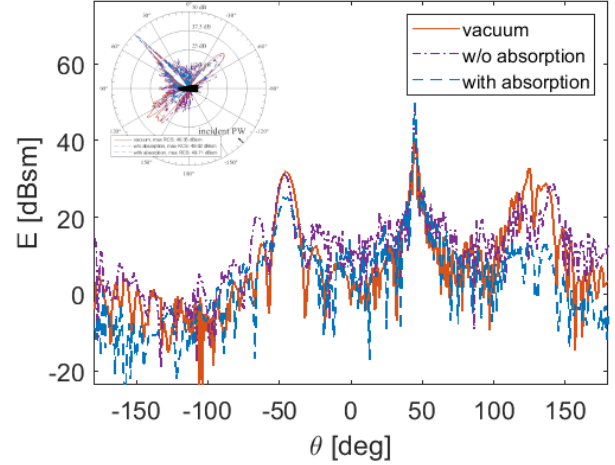


Fig. 18. Bistatic RCS of IXV vehicle at Mach 12, with incidence at $\theta = -135^\circ$. The results compare the RCS for the full plasma (with collisions, solid line) and the collisionless case (dot-dashed line); the results without plasma are also reported for the sake of comparison (dashed line). The same data are also shown in polar format in the inset.

the normalised gradient scale length δ remains below 0.05 and that value is attained for about 10% of the rays over a path of few wavelengths. Similarly, the absorption is maximal in this region, where equation 12 becomes marginally satisfied. On most computational domain, the ray tracing assumptions are very well justified, and thus possible error expected to be small. The ensuing radiation pattern is shown in Fig. 20; the approximate direction of the link toward the ground station (at that point of the IXV trajectory) is indicated with an arrow. The free space radiation pattern is also reported for comparison. The free space pattern (red line) is strongly modified and weakened especially toward the ground direction at $\theta = 180^\circ$ suggesting a black-out or brown-out in the communication. Interestingly, it turns out that here the link direction does not cross a cut-off layer. Hence, the strong attenuation in the radio link is not due to plasma cut-off as typically assumed; the plasma path loss is instead due to a combination of strong ray bending (seen in Fig. 19) and absorption.

Another very interesting analysis is the impact of plasma on navigation, which employed GPS at 1.6GHz in IXV. The GPS link differs from the TM link for the (slightly) different frequency, and especially for the different antenna location, here on the top part of the vehicle. Ray analysis is shown in Fig. 21, and the resulting patterns are shown in Fig. 22. The entire orbit of the IXV experiment is below 100km altitude, so that mostly the upper hemisphere is relevant to assess possible link obstruction; results in Fig. 22 are then displayed on the (u, v) -plane, with $u = \sin(\theta) \cos(\phi)$ and $v = \sin(\theta) \sin(\phi)$.

While the higher density plasma layers are in the bottom part of the vehicle, the plasma is dense and inhomogeneous enough in the entire volume around as to significantly impact on extended angular regions or the antenna pattern. This strong modification of the pattern is seen to be primarily due to strong ray deflection upwards (Fig. 21). In turn, this deflection is due to sustained density gradients for a significant spatial region

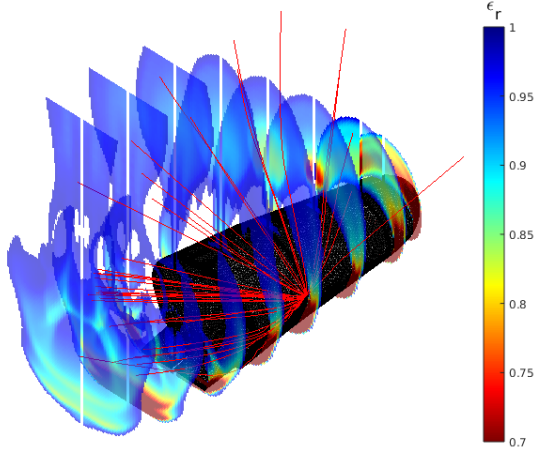


Fig. 19. TM Radiolink at Mach 15: selected ray trajectories, with plasma density overlay. Rays depart from the location of the TM antenna; plasma density is represented as relative permittivity ϵ_r at the frequency of 2.26 GHz with a color plot scale.

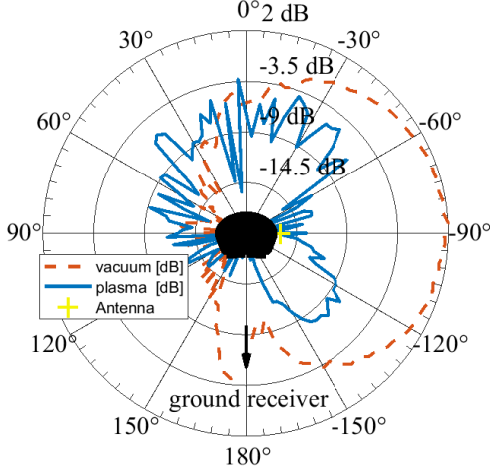


Fig. 20. TM Radiolink at Mach 15: radiation pattern of on-board antenna (co-polar component, RHCP) mounted on the right side of the IXV vehicle. The figure shows the vacuum pattern and the pattern with plasma (with collisional absorption). The direction of the earth receiver is indicated with a black arrow.

(see map), not to near-cutoff effects.

C. Numerical workload and resources

In the real-life cases in this section, computational domains where typically in excess of a $10\text{m} \times 10\text{m} \times 5\text{m}$ box, i.e. $100\lambda \times 100\lambda \times 50\lambda$ at the operational frequency of 2.6GHz. Despite these very large volumes, memory needs are very modest and dominated by the input data such as the CFD plasma grid and the vehicle surface mesh. Indeed, for all simulations reported here we used a standard PC with Intel core-i7 multicore CPU and 32GB of RAM.

In this proposed hybrid scheme most of the computational (CPU) time is spent by ray-tracing in the inhomogeneous

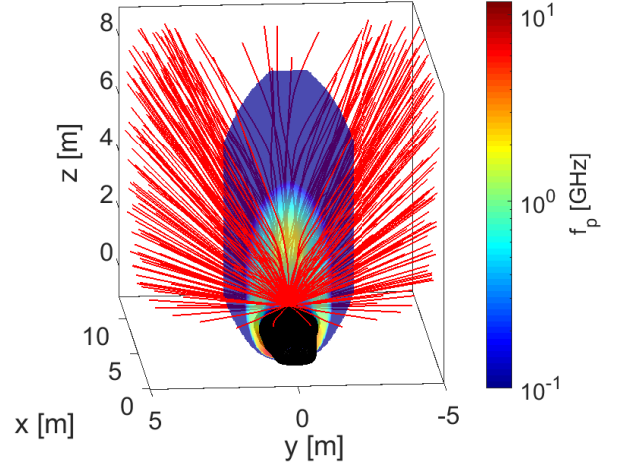


Fig. 21. GPS link at Mach 20: rays originating from the GPS antenna location.

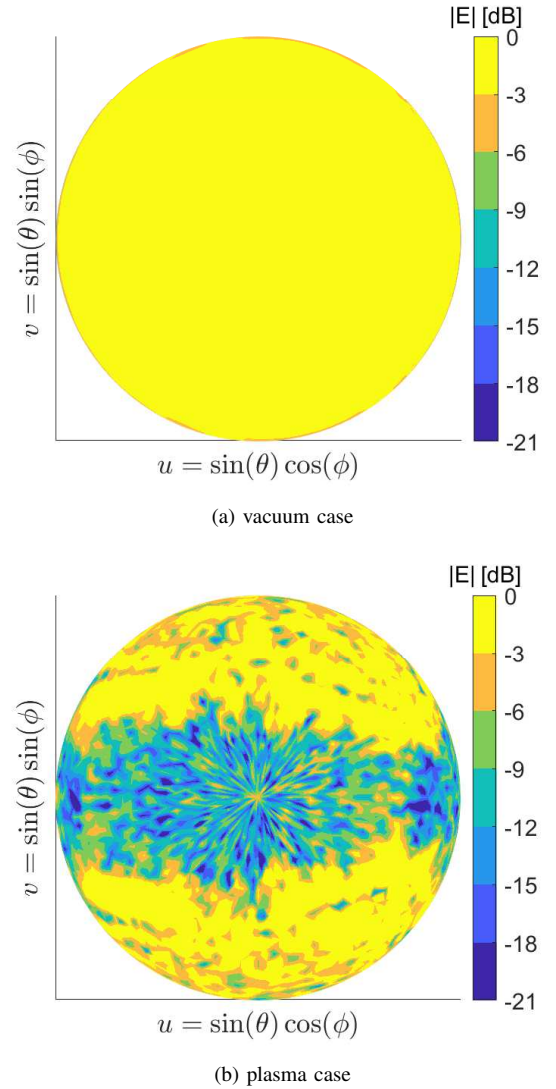


Fig. 22. GPS link at Mach 20: radiation pattern represented as color code on the (far field) sphere to highlight possible impact on GPS satellite links.

plasma, whilst the radiation part only accounts for few percent

of the total CPU time. For the presented cases of complex vehicle and typical sub-wavelength resolution at the Huygens surface (see section II-E) we trace up to 0.5M rays; this requires up to 10-12h on the indicated machine.

We note that ray tracing is very easily parallelized (and so is radiation); this, associated with the low memory requirements, makes the scaling of this approach very favorable towards multi-core or parallel machines like GPUs.

V. CONCLUSIONS

We have presented a method to compute wave scattering and radiation for electrically large objects immersed in a plasma, as the one originating from hypersonic flight conditions. We employ the Eikonal approximation in the large inhomogeneous plasma region, and compute radiation and scattering via Equivalence Theorem. The implementation has been benchmarked against analytical, PO and MoM references. We have employed the approach to analyse bistatic RCS and radio links for a real-life re-entry vehicle, with 3D plasma profiles imported from state of the art fluid dynamic (CFD) simulations. This case study has highlighted the impact of plasma spatial variations, not only its density, on the electromagnetic response; collisional effects have likewise been found important.

Future work regards extension of this method to hybrid Ray-MoM approaches or both installed antennas and for the treatment of fast gradients.

ACKNOWLEDGMENT

This work was supported in part by ESA-ESTEC under contracts No. 4200022989/09/NL/JK “Re-Entry Vehicle Communication Technology”, and 4000112664/14/NL/MH “Mitigation of RF Blackout for Re-Entry Vehicles”.

REFERENCES

- [1] K. Baggaley, “These planes could jet you around the world at hypersonic speed.” available at <https://www.nbcnews.com/mach/science/these-planes-could-jet-you-around-world-hypersonic-speed-ncna843386?cid=related>, 2019.
- [2] K. Baggaley, “This hypersonic airliner would take you from los angeles to tokyo in under two hours.” available at <https://www.nbcnews.com/mach/science/hypersonic-airliner-would-take-you-los-angeles-tokyo-under-two-ncna1045988>, 2018.
- [3] F. Bariselli, S. Boccelli, T. Magin, A. Frezzotti, and A. Hubin, “Aerothermodynamic modelling of meteor entry flows in the rarefied regime,” in *2018 Joint Thermophysics and Heat Transfer Conference*, 2018.
- [4] F. Bariselli, S. Boccelli, B. Dias, A. Hubin, and T. E. Magin, “A self-consistent method for the simulation of meteor trails with an application to radio observations,” *A&A*, vol. 641, p. A100, 2020.
- [5] P. E. Ross, “Flying beyond mach 5 is back, decades after the original need-for-speed arms race ended: Going hypersonic,” *IEEE Spectrum*, vol. 57, pp. 32–37, Dec. 2020.
- [6] N. V. Budko and A. B. Samokhin, “Spectrum of the volume integral operator of electromagnetic scattering,” *SIAM Journal on Scientific Computing*, vol. 28, no. 2, pp. 682–700, 2006.
- [7] L. J. Gomez, A. C. Yücel, and E. Michielssen, “Volume-surface combined field integral equation for plasma scatterers,” *IEEE Antennas and Wireless Propagation Letters*, vol. 14, pp. 1064–1067, Dec 2015.
- [8] A. C. Yücel, L. J. Gomez, and E. Michielssen, “Internally combined volume-surface integral equation for em analysis of inhomogeneous negative permittivity plasma scatterers,” *IEEE Transactions on Antennas and Propagation*, vol. 66, no. 4, pp. 1903–1913, 2018.
- [9] J. W. Qian and M. Y. Xia, “Simulation of scattering by a rotating hypersonic object with plasma sheath,” in *2015 IEEE International Conference on Computational Electromagnetics*, pp. 258–260, 2015.
- [10] J.-W. Qian, H.-L. Zhang, and M.-Y. Xia, “Modelling of Electromagnetic Scattering by a Hypersonic Cone-Like Body in Near Space,” *International Journal of Antennas and Propagation*, vol. 2017, 2017.
- [11] H. Wang, L. Xu, B. Li, S. Descobes, and S. Lanteri, “An exponential-based dgtd method for modeling 3-d plasma-surrounded hypersonic vehicles,” *IEEE Transactions on Antennas and Propagation*, vol. 68, no. 5, pp. 3847–3858, 2020.
- [12] A.-L. Deng and L.-M. Zhang, “Direct solution of the volume integral equation for electromagnetic scattering from dielectric objects with negative permittivity,” *J. Opt. Soc. Am. A*, vol. 38, pp. 1015–1023, Jul 2021.
- [13] H. Sun, J. Wang, Y. Han, Z. Cui, P. Sun, X. Shi, and W. Zhao, “Backward scattering characteristics of a reentry vehicle enveloped by a hypersonic flow field,” *International Journal of Antennas and Propagation*, vol. 2018, 2018.
- [14] Y. Zhong-cai and S. Jia-ming, “Collisional, nonuniform plasma sphere scattering calculation by fdtd,” *International Journal of Infrared and Millimeter Waves*, vol. 28, pp. 987–992, 2007.
- [15] Y. Takahashi, R. Nakasato, and N. Oshima, “Analysis of radio frequency blackout for a blunt-body capsule in atmospheric reentry missions,” *Aerospace*, vol. 3, p. 2, 2016.
- [16] V. I. Sotnikov, J. N. Leboeuf, and S. Mudaliar, “Scattering of electromagnetic waves in the presence of wave turbulence excited by a flow with velocity shear,” *IEEE Trans. Plasma Sci.*, vol. 38, no. 9, p. 2208–2218, 2010.
- [17] V. Sotnikov, T. Kim, J. Lundberg, I. Paraschiv, and T. A. Mehlhorn, “Scattering of electromagnetic waves by vortex density structures associated with interchange instability: Analytical and large scale plasma simulation results,” *Phys. Plasmas*, vol. 21, no. 5, p. 052309, 2014.
- [18] H. Ling, H. Kim, G. A. Hallock, B. W. Birkner, and A. J. M. Zaman, “Effect of an arcjet plume on satellite reflector performance,” *IEEE Transactions on Antennas and Propagation*, vol. 39, no. 9, pp. 1412–1420, 1991.
- [19] H. Kim and L. Ling, “Electromagnetic scattering by inhomogeneous object by ray tracing,” *IEEE Transactions on Antennas and Propagation*, vol. 40, pp. 512–525, May 1992.
- [20] S. D. Benedetto, G. C. Rufolo, and M. Marini, “European space agency intermediate experimental vehicle: Development of an independent aerothermodynamic database tool,” *Proceedings of the Institution of Mechanical Engineers, Part G: Journal of Aerospace Engineering*, vol. 228, no. 3, pp. 435–454, 2014.
- [21] R. Angelini and A. Denaro, “Isv re-entry demonstrator: Mission overview, system challenges and flight reward,” *Acta Astronautica*, vol. 124, pp. 18–30, 2016.
- [22] Z. Cong, Z. He, and R. S. Chen, “An efficient volumetric sbr method for electromagnetic scattering from in-homogeneous plasma sheath,” *IEEE Access*, vol. 7, pp. 90162–90170, 2019.
- [23] S.-H. Liu and L.-X. Guo, “Analyzing the electromagnetic scattering characteristics for 3-d inhomogeneous plasma sheath based on po method,” *IEEE Transactions on Plasma Science*, vol. 44, no. 11, pp. 2838–2843, 2016.
- [24] R. Brem and T. F. Eibert, “A shooting and bouncing ray (sbr) modeling framework involving dielectrics and perfect conductors,” *IEEE Transactions on Antennas and Propagation*, vol. 63, no. 8, pp. 3599–3609, 2015.
- [25] G. Vecchi, M. Sabbadini, R. Maggiora, and A. Siciliano, “Modelling of antenna radiation pattern of a re-entry vehicle in presence of plasma,” in *Antennas and Propagation Society International Symposium*, vol. 1, pp. 181–184, IEEE, New York, NY, USA, 2004.
- [26] M. Bandinelli, L. Pandolfo, J. L. A. Quijano, G. Vecchi, H. Pawlak, and F. Marliani, “An electromagnetic modelling tool for radio frequency interference caused by plasma plumes,” in *2011 IEEE International Symposium on Electromagnetic Compatibility*, pp. 635–640, 2011.
- [27] L. Pandolfo, M. Bandinelli, J. L. A. Quijano, G. Vecchi, H. Pawlak, and F. Marliani, “Em modelling of rf propagation through plasma plumes,” in *2012 ESA Workshop on Aerospace EMC*, pp. 1–7, 2012.
- [28] C. Park, “Review of chemical-kinetic problems of future nasa missions - i: Earth entries,” *Journal of Thermophysics and Heat Transfer*, vol. 7, no. 3, pp. 385–398, 1993.
- [29] C. Park, R. Jaffe, and H. Partridge, “Chemical-Kinetic Parameters of Hyperbolic Earth Entry,” *Journal of Thermophysics and Heat Transfer*, vol. 15, no. 1, pp. 76–90, 2001.

- [30] E. Levin and M. Wright, "Collision Integrals for Ion-Neutral Interactions of Nitrogen and Oxygen," *Journal of Thermophysics and Heat Transfer*, vol. 18, pp. 143–147, January-March 2004.
- [31] M. Wright and E. Levin, "Collision Integrals for Ion-Neutral Interactions of Air and Argon," *Journal of Thermophysics and Heat Transfer*, vol. 19, pp. 127–128, January-March 2005.
- [32] M. Wright, D. Bose, G. Palmer, and E. Levin, "Recommended Collision Integrals for Transport Property Computations, Part 1: Air Species," *AIAA Journal*, vol. 43, pp. 2558–2564, December 2005.
- [33] R. N. Gupta, J. M. Yos, R. A. Thompson, and K. P. Lee, "A review of reaction rates and thermodynamic and transport properties for an 11-species air model for chemical and thermal nonequilibrium calculations to 30000 K," techreport NASA RP-1232, NASA, Washington, DC, USA, 1990.
- [34] D. D'Ambrosio and D. Giordano, "Electromagnetic fluid dynamics for aerospace applications and heat transfer," *Journal of Thermophysics and Heat Transfer*, vol. 21, no. 2, pp. 284–302, 2007.
- [35] D. D'Ambrosio, D. Giordano, and D. Bruno, "Fully coupled maxwell/navier-stokes simulation of electromagnetic hypersonics including accurate transport models," in *40th AIAA Plasmadynamics and Lasers Conference*, 2009.
- [36] T. H. Stix, *Waves in Plasmas*. Springer, 1992.
- [37] K. G. Budden, *Radio Waves in the Ionosphere*. Cambridge University Press, 1961.
- [38] L. D. Landau, E. M. Lifshitz, and L. P. Pitaevskii, *Statistical Physics*, vol. 1. Oxford: Pergamon Press, 1980.
- [39] D. W. Lankford, "A study of electron collision frequency in air mixtures and turbulent boundary," tech. rep., Air Force Weapons Laboratory Kirtland Air Force Base, New Mexico, 1972.
- [40] M. Born and E. Wolf, *Principles of Optics*, vol. 6. Pergamon, sixth edition ed., 1980.
- [41] Y. A. Kravtsov and Y. I. Orlov, *Geometrical Optics of Inhomogeneous Media*, vol. 6 of *Serie on Wave Phenomena on Wave Phenomena Serie on Wave Phenomena*. Berlin: Springer, 1990.
- [42] H. Bremmer and S. W. Lee, "Propagation of a geometrical optics field in a isotropic inhomogeneous medium," *Radio Sci*, vol. 19, pp. 243–257, 1984.
- [43] I. B. Bernstein, "Geometric optics in space- and time-varying plasmas," *The Physics of Fluids*, vol. 18, no. 3, pp. 320–324, 1975.
- [44] R. M. Jones, "Ray theory for lossy media," *Radio Science*, vol. 5, pp. 793–801, 1970.
- [45] D. Censor and Y. Gavan, "Wave packets, group velocities and rays in lossy media, revisited," in *16th. Convention of Electrical and Electronics Engineers in Israel, Tel Aviv*, 1989.
- [46] M. Brambilla and A. Cardinali, "Eikonal description of hf waves in toroidal plasmas," *Physics of Plasmas*, vol. 24, p. 1187, 1982.
- [47] W. C. Gibson, *The Method of Moments in Electromagnetics*. Chapman & Hall/CRC, 2008.
- [48] M. Li, M. A. Francavilla, R. Chen, and G. Vecchi, "Wideband fast kernel-independent modeling of large multiscale structures via nested equivalent source approximation," *IEEE Trans. Antennas Propagat*, vol. 63, p. 5, 2015.
- [49] G. Ruck, *Radar Cross Section Handbook*. Plenum Press, 1970.
- [50] C. A. Balanis, *Advanced engineering electromagnetics*. New York: Wiley, 2nd ed., 2012.
- [51] W. Gibson, "Scattered field of a conducting and stratified spheres."
- [52] J. R. Wait and C. M. Jackson, "Calculations of the bistatic scattering cross section of a sphere with an impedance boundary condition," *RADIO SCIENCE*, vol. 69, February 1965.